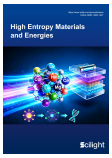
High Entropy Materials and Energies
https://www.sciltp.com/journals/heme



Article

Check for updates

Fabrication and Characterization of High-Temperature Superconducting $Bi_{2-x}Pb_xSr_2Ca_2Cu_3O_{10+\gamma}$ Tapes

Diego André Orna Tiburcio [1,2], Henry E. Sanchez Cornejo [1,*], Jorge García Dulanto [1], Melvin James Godoy [1], Angel G. Bustamante Domínguez [1], Jesus Flores Santibañez [1], Juan Carlos González [1], Santos Ricardo Celis Rojas [3], Crispin H. W. Barnes [4] and Luis De Los Santos Valladares [4,5,6,*]

[1] Laboratorio de Cerámicos y Nanomateriales, Facultad de Ciencias Físicas, Universidad Nacional Mayor de San Marcos, Lima 15081, Perú
[2] Laboratório de Microscopia Eletrônica de Alta Resolução, Centro de Caracterização Avançada para Indústria de Petróleo (LaMAR/CAIPE), Universidade Federal Fluminense, Niterói 24210-346, Brazil
[3] Facultad de Ingeniería, Universidad Nacional de Barranca, Barranca 15169, Peru
[4] Cavendish Laboratory, Department of Physics, University of Cambridge, Cambridge CB3 0US, UK
[5] Department of Physics, Al-Farabi Kazakh National University, Almaty 050040, Kazakhstan
[6] Institute of Physical and Technical Sciences, L.N. Gumilyov Eurasian National University, Astana 010000, Kazakhstan
* Correspondence: henry.sanchez@unmsm.edu.pe (H.E.S.C.), ld301@cam.ac.uk (L.D.L.S.V.)

How To Cite: Orna Tiburcio, D.A.; Sanchez Cornejo, H.E.; Dulanto, J.G.; et al. Fabrication and Characterization of High-Temperature Superconducting $Bi_{2-x}Pb_xSr_2Ca_2Cu_3O_{10+\gamma}$ Tapes. *High Entropy Materials and Energies* **2026**, *1*(1), 7. https://doi.org/10.53941/heme.2026.100007

Received: 24 May 2026
Revised: 24 September 2026
Accepted: 19 October 2026
Published: 3 November 2026

Abstract: This work reports the fabrication and comprehensive characterization of $Bi_{2-x}Pb_xSr_2Ca_2Cu_3O_{10+\gamma}$ superconducting tapes with coexistence of Pb-doped Bi-2223 and Bi-2212 phases, embedded in a high-purity silver matrix. The tapes were produced by the powder-in-tube (PIT) method, followed by heat treatments at 865 and 810 °C and mechanical lamination, yielding homogeneous tapes with a thickness of about 0.6 mm. Structural analysis by X-ray diffraction shows that the precursor powder consists mainly of the BPSCCO-2223 phase and a carbonate secondary phase, whereas the tape core additionally contains the BPSCCO-2212 phase, Ca_2PbO_4 and $Ca_{2.675}Cu_3Pb_{0.535}Sr_{2.675}Bi_{1.6}O_x$. SEM-EDS confirms the flattening and alignment of grains after rolling, the presence of Ca- and Pb-rich secondary phases, and the absence of detectable silver diffusion into the core. DC susceptibility measurements under 50 and 1000 Oe reveal two superconducting transitions in the core, associated with the 2223 and 2212 phases, and a clear reduction of the irreversibility temperature with respect to the powder. From hysteresis loops, the critical fields (H_{C1} and H_{irr}) and the vortex-matter $B-T$ phase diagrams were constructed, showing a shift of the irreversibility line to lower fields and temperatures for the tape core. The critical current density estimated with the Bean model reaches values of the order of 10^5 A/cm^2 at 10 K for the tape core, with the enhancement attributed to grain alignment and secondary-phase pinning. Magnetic relaxation measurements show a complex, two-plateau decay in the core at 5 K, attributed to the competition between the coexisting 2223 and 2212 phases. The results provide a complete picture of the microstructural, magnetic and transport behaviour of Pb-doped Bi-2223 tapes and establish a basis for their optimisation.

Keywords: superconductivity; superconducting tapes; vortex dynamics

1. Introduction

Since the discovery of high-temperature superconductors (HTS), superconducting tapes and wires have become key candidates for electric power transmission, high-field magnets, motors, generators, fault current

Copyright: © 2026 by the authors. This is an open access article under the terms and conditions of the Creative Commons Attribution (CC BY) license (https://creativecommons.org/licenses/by/4.0/).
Publisher's Note: Scilight stays neutral with regard to jurisdictional claims in published maps and institutional affiliations.

limiters, magnetic resonance imaging (MRI), nuclear magnetic resonance (NMR), magnetic levitation and fusion energy systems [1–3]. Among the different HTS families, cuprate superconductors remain the most mature for practical conductors, and their performance depends strongly on the material composition, microstructure, grain alignment, and flux-pinning landscape [3,4].

First-generation (1G) HTS tapes based on the Bi-Sr-Ca-Cu-O system, especially the Pb-doped Bi-2223 phase, have attracted considerable attention because of their high critical temperature, above 100 K and their established powder-in-tube (PIT) fabrication route [4,5]. Bi-2223/Ag tapes can operate at liquid-nitrogen temperatures and offer important advantages over second-generation REBCO coated conductors, including lower raw-material and processing costs, high reproducibility and scalability to long-length production [3,4]. Pb doping is essential in this system because it stabilises the Bi-2223 phase, accelerates its formation, improves grain connectivity, and introduces defects that can act as effective flux-pinning centres [2,6,7]. These features make Pb-doped Bi-2223 tapes attractive for practical applications operating under moderate cryogenic conditions, even though their in-field performance is generally lower than that of REBCO tapes [3,4].

The structural, morphological, and superconducting properties of 1G Bi-2223 tapes depend sensitively on several thermal and mechanical variables involved in their fabrication by PIT. These include the precursor composition and calcination conditions, milling, filling density, heat-treatment temperature and dwell time, oxygen partial pressure, heating and cooling rates, intermediate rolling or pressing and post-rolling annealing [6–8]. Such variables control phase evolution, grain alignment, core density, porosity, secondary-phase formation, intergranular connectivity, crack formation and possible Ag diffusion into the superconducting core. In particular, the coexistence of the Bi-2223 and Bi-2212 superconducting phases is of great interest because the lower-T_C Bi-2212 phase can influence current percolation, weak-link behaviour, vortex dynamics, irreversibility line and the transport current capabilities of the tape [5,8,9]. The interplay between these two superconducting phases, together with secondary phases and defects, defines the effective pinning landscape and the vortex phase diagram [9–11].

Therefore, the aim of this work is to fabricate and comprehensively characterise $Bi_{2-x}Pb_xSr_2Ca_2Cu_3O_{10+\gamma}$ superconducting tapes with coexistence of Pb-doped Bi-2223 and Bi-2212 phases, embedded in a high-purity silver matrix. The tapes are produced by the PIT method, followed by heat treatments at 865 and 810 °C and mechanical lamination to obtain homogeneous tapes with a thickness of about 0.6 mm. The precursor powder and the superconducting core extracted from the tape are compared using X-ray diffraction, scanning electron microscopy coupled with energy-dispersive X-ray spectroscopy, DC magnetic susceptibility, hysteresis loops, and magnetic relaxation measurements. The structural and magnetic analyses allow the identification of the main phases, the superconducting transition temperatures, the irreversibility temperatures, the critical fields, the vortex phase diagrams and the critical current densities estimated from the Bean model [9,12,13]. The results provide a picture of the microstructural and magnetic behaviour of Pb-doped tapes and establish a basis for their optimisation.

The findings are relevant to potential applications of Pb-doped Bi-2223 and Bi-2212 tapes in power cables, current leads, high-field magnets, MRI/NMR systems, fault current limiters, magnetic levitation, and fusion-related devices [3,4,14,15]. In particular, the possibility of operating these tapes at liquid-nitrogen or intermediate cryogenic temperatures, together with their mature and scalable PIT fabrication, makes them promising for large-scale superconducting systems where cost, reproducibility, and long-length conductor availability are critical [3,4,15]. Understanding the phase coexistence, pinning mechanisms, and vortex dynamics in these tapes is therefore important for further improving their transport performance and extending their operational range.

2. Experimental

The superconducting tapes were fabricated by the powder-in-tube (PIT) method, as summarised in Figure 1. The precursor powder was a commercial Pb-doped Bi-2223 compound with nominal composition $Bi_{1.6}Pb_{0.4}Sr_{1.6}Ca_{2.0}Cu_{2.8}O_{9.2+x}$ (Sigma-Aldrich (Louis, MO, USA), reference code 378720). The precursor was received in the form of fragile, opaque grey spheres. On the other hand, high-purity silver tubes (99.95%, GoodFellow) with an external diameter of 2.00 mm were cut into 75 mm long pieces and stored under isopropyl alcohol before use.

Following, 9 g of the precursor granules were ground in an agate mortar and pestle for 3 h (Figure 1b). Part of the resulting powder was used for X-ray diffraction (XRD) characterisation, while another part was pressed into control pellets. These pellets were prepared with 0.1 g of powder under 6 tons of pressure for 5 min, giving a thickness of approximately 0.3 mm (Figure 1c). The control pellets were used as qualitative references to monitor the effect of the thermal ramps and to detect possible melting or decomposition of low-melting phases.

The remaining powder was used to fill the silver tubes. One end of each tube was sealed by bending and folding under pressure to create a stop (Figure 1d). The fine powder was introduced using two catheters, pre-sealed

needles and a fixed-blade surgical needle (Figure 1e). After filling, the opposite end was folded and sealed. The tubes were then weighed to determine the mass of the powder core. Each tube, together with its control pellet, was placed in a refractory tray for the first heat treatment in a Lenton Thermal Designs tubular furnace (Figure 1f). The thermal profile consisted of a heating ramp of 5 °C/min up to 865 °C, a dwell of 15 h, and subsequent cooling to room temperature.

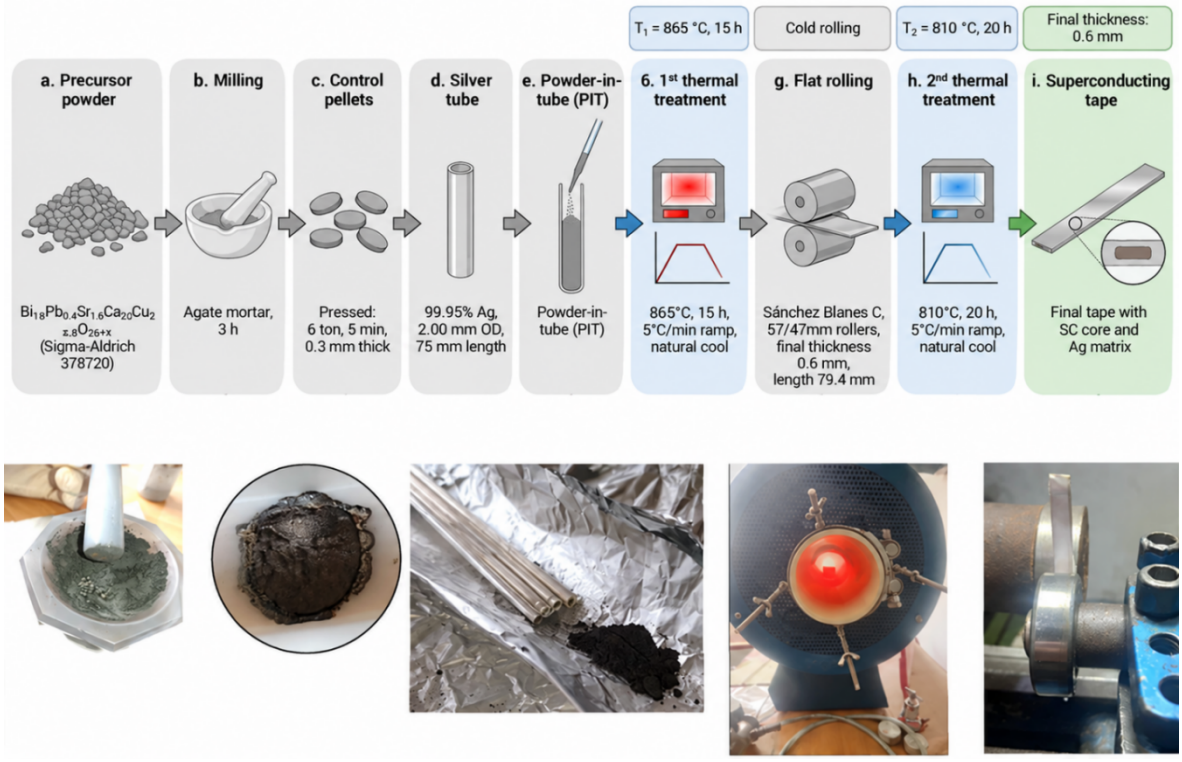


Figure 1. Step-by-step fabrication of BPSCCO-2223 superconducting tapes by the powder-in-tube method. (**a**) Precursor powder. (**b**) Milling in an agate mortar. (**c**) Control pellets. (**d**) Sealing of one end of the silver tube. (**e**) Filling of the tube with precursor powder. (**f**) First thermal treatment at 865 °C for 15 h. (**g**) Flat rolling. (**h**) Second thermal treatment at 810 °C for 20 h. (**i**) Final superconducting tape; the inset shows a cross-sectional view of the core/Ag matrix.

The control pellets provided important information about the thermal stability of the precursor. After the first treatment, the pellets had lost their original shape, showed a golden coloration, adhered to the tray, and became harder than the refractory tray. These observations indicate that 865 °C is close to the melting temperature of some low-melting components of the precursor. In addition, material leakage was observed from the pressure-sealed ends of the silver tubes, which stained the boat with gold and silver tones. These effects justified the use of a lower temperature for the post-rolling annealing, as described below.

After the first heat treatment, the tubes were laminated using a Sánchez Blanes model C mechanical lathe. Bearings of 57 mm were adapted to the main axis and 47 mm to the mobile arm. As the space between the bearings was reduced, the tubes were progressively flattened (Figure 1g). Homogeneous tapes with a thickness of 0.6 mm and a length of 79.4 mm were obtained. The lamination process promotes grain alignment and densification of the superconducting core, but it also introduces internal stresses and microcracks.

To relieve these stresses, repair cracks, and improve intergranular connectivity, a second heat treatment was carried out on the laminated tapes. The samples were heated at 5 °C/min to 810 °C, held for 20 h, and then cooled slowly to room temperature (Figure 1h). Slow cooling was used to reduce residual stress and to promote the formation of larger crystals. After this second treatment, the final superconducting tape was obtained (Figure 1i).

The evolution of the sample mass during fabrication was monitored by weighing the silver tube, the tube plus powder core, and the core alone after each thermal treatment. Table 1 summarizes the masses obtained after stuffing, after the first heat treatment (865 °C, 15 h), and after the second heat treatment (810 °C, 20 h). The mass of the silver tube remained constant at 0.949 g, confirming that no silver was lost because the working temperatures are well below the melting point of silver (962 °C). This is further supported by the EDS analysis presented in Section 3.2, which shows no detectable silver diffusion into the superconducting core. Therefore, the mass of the core could be reliably obtained by subtracting the mass of the silver matrix from the total mass of the tape.

The core mass decreased from 0.2091 g after stuffing to 0.1627 g after the first heat treatment, corresponding to a loss of 18.1% relative to the initial core mass. After the second heat treatment, the core mass decreased further to 0.1578 g, giving a total loss of 24.5%. The most significant mass loss occurred during the first heat treatment, mainly due to the decomposition of carbonates and the release of volatile components [16,17]. The additional loss during the second treatment was much smaller, indicating that most volatile by-products had already been removed. These results are visualised in Figure 2, which plots: (i) the mass of the ribbon (core + Ag); (ii) the core alone; and (iii) the percentage changes between stages.

Table 1. Comparison of mass content in grams and percentage during the manufacturing process of superconducting tapes.

Process	m-Ag (g)	Matrix+Core(g)	m-Core (g)	% mass
Stuffed	0.949	1.1581	0.2091	18.055
1st TT	0.949	1.1117	0.1627	14.635
2nd TT	0.949	1.1068	0.1578	14.257

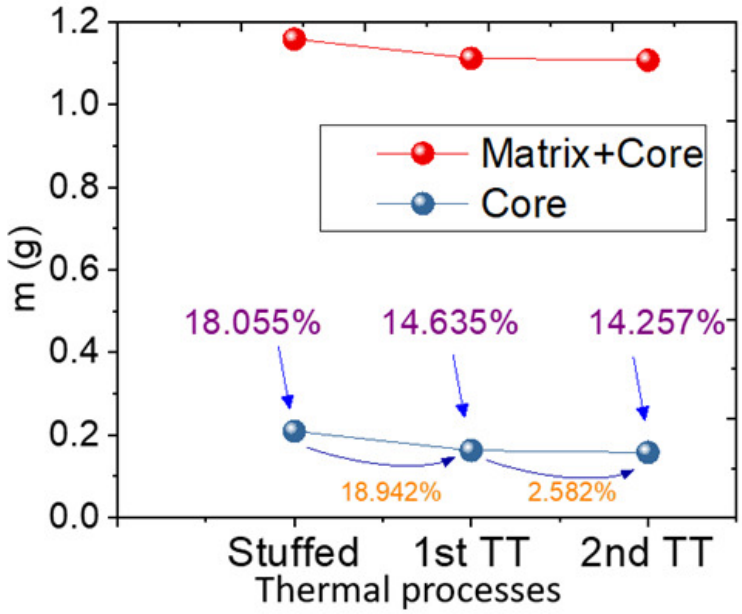


Figure 2. Graph showing the evolution through the processes for the masses of the ribbon (red), core (blue), variation of Core mass with respect to Ribbon (Purple), and variation with respect to the masses of the Core (orange).

To extract samples from the core of the silver matrix, the tapes were cut with steel pliers to a length of about 5 mm. Lateral pressure was applied with hemostatic forceps to open the silver matrix. The pressure was increased until the lateral fracture of the core was felt, and then light pressure was applied in the same direction of the tape to release the core. The material was extracted in the form of small flakes of approximately 1 mm^2, together with residual powder. These flakes were used for the subsequent structural, morphological, and magnetic characterisation.

The structural characterisation was performed by X-ray diffraction (XRD) technique. The data was collected from 20° to 50° (0.02° step) using a powder universal diffractometer Bruker AXS D8 Focus with Cu $K_{\alpha 1}$ radiation (λ =1.54056 Å).

For the morphological and chemical composition analysis, the Scanning Electron Microscope (SEM) ThermoScientific Prisma E was used at 2000× and 8000× magnification, with an acceleration voltage of 30 kV. Elemental mapping was carried out using an energy-dispersive X-ray spectroscopy (EDS) detector coupled to the SEM.

The magnetisation measurements were performed using a Quantum Design DC-MPMS-SQUID magnetometer equipped with a 7 T superconducting magnet. For all measures the magnetic field was applied along the *c*-axis. The superconducting transition temperature (T_C) was determined from temperature-dependent measurements of M under H_{ext} = 50 and 1000 Oe. The $M(H)$ hysteresis loops measurements were done in a field range 0–5.5 T at 10, 20, 30, 50 and 60 K. Magnetic relaxation measurements were also performed with the DC-MPMS-SQUID magnetometer. The samples were field-cooled at T = 5 and 100 K under a 1 T applied magnetic field. The H_{ext} was then suppressed, and the decay of the magnetisation was measured with time. The field ramp rate was 500 Oe/s.

3. Results and Discussion

3.1. Analysis by X-ray Diffraction

Figure 3 shows the XRD patterns of the precursor powder sample (Figure 3a) and the superconducting core extracted from the tape (Figure 3b). In the precursor powder, two main crystalline phases are identified: the superconducting BPSCCO-2223 (COD card number 1540770) phase and the carbonate phase $(BiPb)_2Sr_{3.5}Cu_2O_8(CO_3)$ (ICSD card number 01-082-0154). The most intense reflections appear at $2\theta = 33.15°$ and 28.02°, which can be assigned to the (117) plane of the BPSCCO-2223 phase and to the (107) plane of the carbonate phase, respectively. The presence of the BPSCCO-2223 phase in the precursor is confirmed by the presence of several reflections belonging to this phase, as can be seen in Figure 3a. Also, the presence of the carbonate phase indicates that the commercial precursor is not phase-pure and that carbonate groups remain in the starting material. This is relevant because such secondary phases can disrupt grain connectivity and reduce the effective superconducting volume fraction.

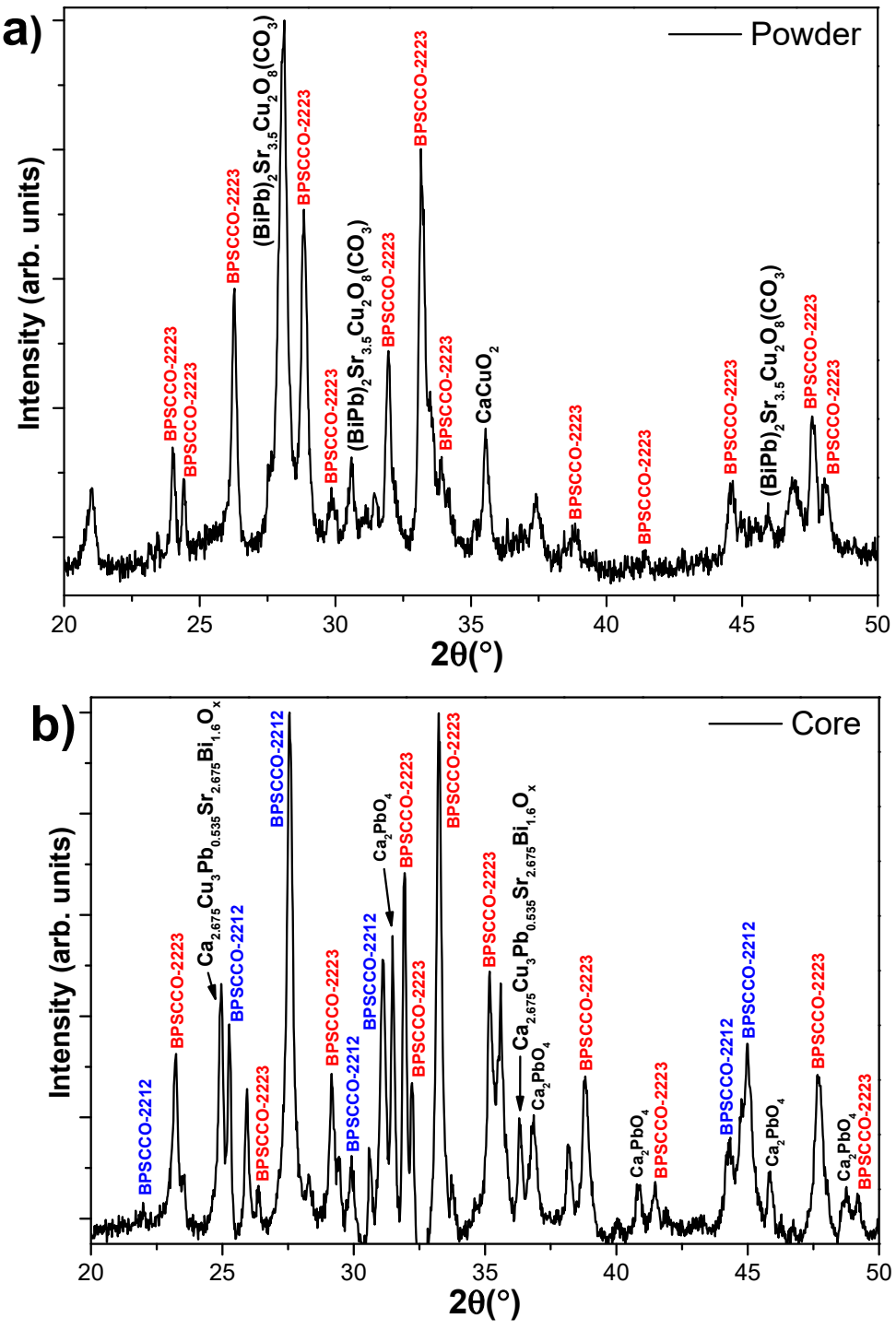


Figure 3. XRD patterns for the powder (**a**) and core (**b**) samples.

In the core sample (Figure 3b), the XRD pattern reveals a more complex multiphase composition. The BPSCCO-2223 phase coexists with the BPSCCO-2212 phase, and two additional secondary phases are detected: Ca_2PbO_4 (ICDD card number 00-048-1533) and $Ca_{2.675}Cu_3Pb_{0.535}Sr_{2.675}Bi_{1.6}O_x$ (ICDD card number 00-046-0644). The main diffraction peaks at 2θ = 27.55 and 33.23 are assigned to the (115) plane of the Bi(Pb)-2223 phase and to the (111) plane of the Bi(Pb)-2212 phase, respectively. Other characteristic reflections of the 2223 and 2212 phases are also observed, confirming the coexistence of both superconducting phases in the tape core. It should be noted that although the low-angle (001) reflection of the 2223 phase at 2θ ≈ 4.8° falls outside the measured 2θ range (20−50°), the presence of the 2223 phase in the core is unambiguously supported by several higher-angle reflections of this phase observed in Figure 3b, as well as by the magnetic susceptibility measurements discussed below, which show two superconducting transitions in the core sample: $T_{C(onset)}^{2223}$ and $T_{C(onset)}^{2212}$.

The formation of 2212 and carbonate-related secondary phases can be attributed to the thermal treatments. At 865 and 810 °C, the 2223 phase may partially decompose, and the subsequent cooling may not fully restore the 2223 stoichiometry. In addition, Pb loss or redistribution and reaction with CO_2 or moisture can promote the segregation of secondary phases. Therefore, the tape core is not a single-phase 2223 superconductor but a multiphase composite in which 2223 and 2212 grains coexist with carbonate-based and Ca-rich secondary phases.

3.2. Analysis by Scanning Microscopy (SEM)

Figure 4 shows the SEM micrographs and EDS elemental maps of the powder and the core-tape sample. The precursor powder consists of irregular, agglomerated grains with a broad size distribution. At 2000× magnification (Figure 4a), the powder exhibits smooth-edged regions together with dispersed sharp and elongated structures on a homogeneous background. The inset grain-size histogram gives an average size of approximately 10.5 μm. This morphology is also observed in Figure 4b, which is consistent with the milling step in an agate mortar and with the presence of a fraction of carbonate secondary phase, as detected by XRD. The EDS mapping in Figure 4c reveals carbon-rich regions distributed throughout the powder. These regions correlate with the sharp and elongated structures and support the presence of $(BiPb)_2Sr_{3.5}Cu_2O_8(CO_3)$.

The elemental composition of the powder (Table 2) is dominated by O (52.2%), C (24.6%), Cu (7.2%), Ca (6.2%), Bi (3.9%), Sr (3.1%) and Pb (0.9%). Minor amounts of Al (1.8%) and Fe (0.2%) are also detected, likely originating from the milling or sample preparation. The high carbon content is consistent with the carbonate phase identified by XRD and indicates that the precursor is not phase-pure.

Table 2. Elemental composition for the powder and core-tape samples.

Sample	Element	Atomic (%)	Atomic % Error	Weight (%)	Weight % Error
Powder	O	52.2	0.3	26.3	0.1
	Cu	7.2	0	14.4	0.0
	Ca	6.2	0	7.9	0.0
	Bi	3.9	0.1	25.9	0.5
	Sr	3.1	0	8.5	0.1
	Al	1.8	0	1.5	0.0
	Pb	0.9	0.1	5.9	0.4
	Fe	0.2	0	0.3	0.0
	C	24.6	0.1	9.3	0.0
Core	O	45.4	0.5	15.6	0.2
	Pb	1.9	0	8.6	0.8
	C	21.3	0.2	5.5	0.1
	Ca	7.3	0.1	6.3	0.0
	Cu	8.8	0	12.1	0.0
	Bi	8.8	0.1	39.1	1.0
	Sr	6.5	0.1	12.3	0.1

After PIT processing and flat rolling, the core-tape sample shows a markedly different morphology (Figure 4d,e). The grains are flattened and elongated, and compacted into a denser microstructure. This change is attributed to the flat-rolling process, which promotes grain alignment, densification, and better packing of the superconducting core. Some flakes detached from the larger structures are observed, together with small particles of about 4 μm decorating the surface of larger grains. The EDS mapping in Figure 4f indicates that these small particles are associated with Ca- and Pb-rich regions, and with carbon-rich areas, in agreement with the Ca_2PbO_4 and carbonate-related phases detected by XRD. The larger flattened grains are associated with the Bi(Pb)-2223 and Bi(Pb)-2212 superconducting phases.

The elemental composition of the core tape (Table 2) shows O (45.4%), C (21.3%), Cu (8.8%), Bi (8.8%), Ca (7.3%), Sr (6.5%) and Pb (1.9%). Compared with the precursor powder, the core exhibits a relative increase in Bi, Sr, Cu and Pb, and a decrease in O and C. This is consistent with the loss of volatile carbonaceous species during the thermal treatments, as also reflected in the mass loss discussed in Section 2.1. The carbon signal remains significant, indicating that carbonate secondary phases are still present in the core after processing. The presence of such phases can reduce the effective superconducting volume and disrupt intergranular connectivity, which is consistent with the reduced diamagnetic shielding observed in the core-tape sample at high magnetic fields [18].

Importantly, no silver is detected in the EDS spectra or elemental maps of the core-tape sample (Figure 4f and Table 2). This confirms that the silver matrix does not diffuse into the superconducting core under the present thermal and mechanical conditions. Therefore, the core mass can be reliably obtained by subtracting the mass of the silver matrix from the total tape mass, as described in Section 2.1. The absence of Ag diffusion also indicates that the superconducting properties of the core are not affected by Ag contamination.

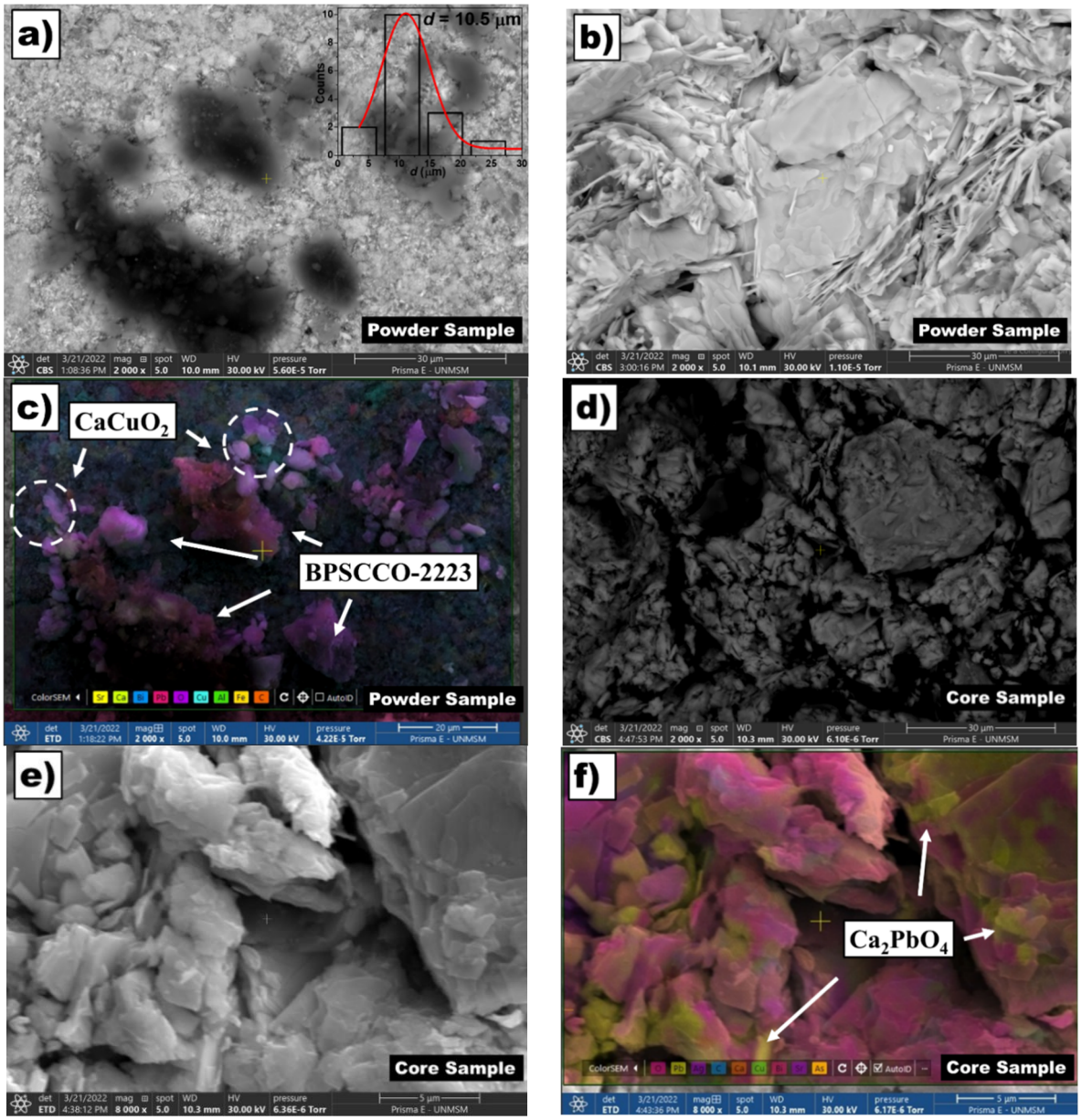


Figure 4. SEM micrographs and EDS elemental mapping of the precursor powder and the core-tape sample. (**a**) Powder at 2000× (site 1); the inset shows the grain-size distribution with an average size of about 10.5 µm. **(b)** Powder at 2000× (site 2). (**c**) EDS mapping of the powder showing carbon-rich regions associated with the carbonate phase. (**d**) and (**e**) Core-tape sample at 2000× and 8000×, showing flattened and elongated grains, detached flakes and small particles. (**f**) EDS mapping of the core showing Ca- and Pb-rich regions associated with Ca_2PbO_4 and carbonate-related secondary phases. No Ag signal is detected in the core.

3.3. Magnetic Properties

3.3.1. DC Magnetic Susceptibility

The magnetic properties were studied using Equation (1), which is used to obtain the magnetic susceptibility (χ) from the data of the magnetic dipole moment (m) measurements carried out on a DC Magnetic Property Measurement equipment. System (DC-MPMS-SQUID) [19].

$$\chi = \frac{M \times W_{molecular}}{H_{ext} \times Mass_{sample}} \quad (1)$$

where $W_{molecular}$ is the molecular weight of the measured sample, H_{ext} is the applied magnetic field and $Mass_{sample}$ is the mass of the sample. Measurements were performed in zero-field-cooling (ZFC) and field-cooling (FC) modes. The irreversibility temperature T_{irr} is defined as the temperature at which the ZFC and FC curves separate, marking the crossover between reversible and irreversible magnetic behaviour [20].

Figure 5a shows the $\chi(T)$ curves for the precursor powder. Under H_{ext} = 50 Oe, a single sharp superconducting transition is observed with $T_{C\ (Onset)}$ = 110 K and T_{irr} = 94 K. When the field is increased to 1000 Oe, both characteristic temperatures decrease to $T_{C\ (Onset)}$ = 106 K and T_{irr} = 75 K. The presence of a single transition is consistent with the XRD results, which show that the precursor powder is mainly composed of the BPSCCO-2223 phase and a carbonate secondary phase, with no significant amount of the 2212 phase.

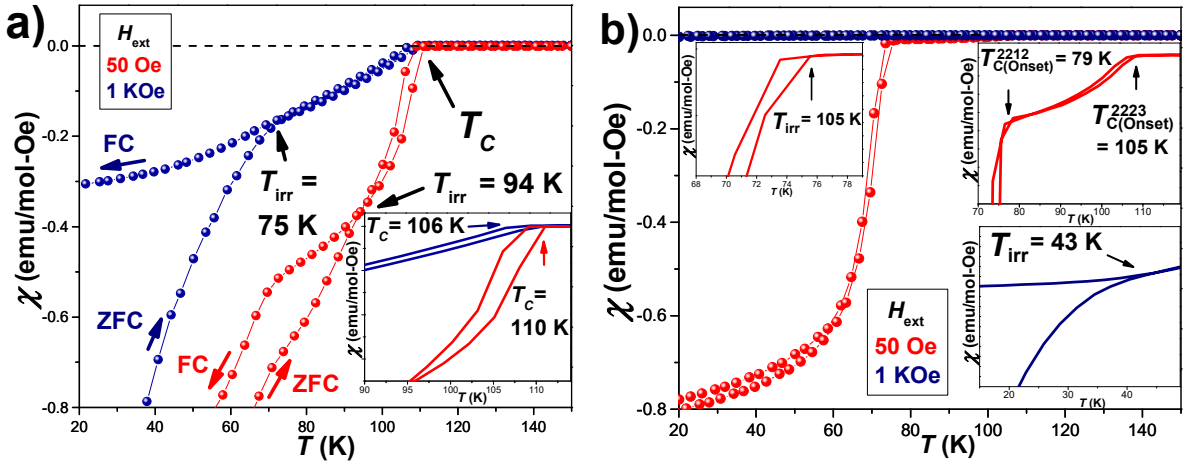


Figure 5. Temperature dependence of DC susceptibility obtained for (**a**) the precursor powder and (**b**) core sample of the superconducting tape.

Figure 5b shows the corresponding $\chi(T)$ curves for the core sample. Under H_{ext} = 50 Oe, two superconducting transitions are resolved: one at $T_{C\ (Onset)}^{2223}$ = 105 K and another at $T_{C\ (Onset)}^{2212}$ = 79 K. The irreversibility temperature is T_{irr} = 75 K. The coexistence of these two transitions is consistent with the XRD analysis of the core, which confirms the simultaneous presence of the 2223 and 2212 phases. It is also consistent with the SEM-EDS results, which reveal Ca- and Pb-rich secondary phases and carbonate inclusions without detectable Ag diffusion into the core [18]. Under H_{ext} = 1000 Oe, the 2223 transition is $T_{C\ (Onset)}^{2223}$ = 104 K, while the 2212 transition shifts down to $T_{C\ (Onset)}^{2212}$ = 78 K and T_{irr} decreases to 43 K.

The characteristic temperatures obtained from the susceptibility analysis are summarised in Table 3. The core sample exhibits a clear reduction of T_{irr} with respect to the precursor powder at both applied fields: from 94 K to 75 K at 50 Oe, and from 75 K to 43 K at 1000 Oe. This reduction indicates a weakening of vortex stability and a narrowing of the irreversible regime in the tape core. It is attributed to the coexistence of the 2212 phase, the presence of secondary phases and carbonate inclusions, and the resulting reduction of the effective superconducting volume and intergranular connectivity.

Table 3. Characteristic temperatures obtained from susceptibility analysis for powder and core samples.

Sample	**Powder**		**Core**			
Phase	**BPSCCO-2223**		**BPSCCO-2223**		**BPSCCO-2212**	
H_{ext}	**50 Oe**	**1000 Oe**	**50 Oe**	**1000 Oe**	**50 Oe**	**1000 Oe**
$T_{C\ (Onset)}$	110 K ± 0.33 K	106 K ± 0.66 K	105 K ± 0.33 K	104 K ± 0.65 K	79 K ± 0.31 K	78 K ± 0.62 K
T_{irr}	94 K ± 0.33 K	75 K ± 0.32 K	75 K ± 0.31 K	43 K ± 0.30 K	75 K ± 0.31 K	43 K ± 0.30 K

3.3.2. $B-T$ Phase Diagram

Magnetisation measurements as a function of the applied magnetic field, $M(H)$ hysteresis loops, were performed to estimate the transport capabilities and the experimental conditions relevant for potential applications. The hysteresis loops are shown in Figure 6a,b for the powder and core samples, respectively. From the $M(H)$ curves, the critical fields were determined for both samples. The low-field regions used to identify $H_{C1}(T)$ are displayed in Figure 6c,d for the powder and core samples, respectively. At low applied fields, Figure 6c,d shows a linear dependence of the magnetization on the magnetic field, corresponding to a reversible magnetization M_{rev}. As the field increases, this linearity is lost and an irreversible magnetization M_{irr} emerges. The field at which the linear dependence disappears is defined as the lower critical field H_{C1} [21]. At high applied fields, the irreversibility field H_{irr} was estimated as the magnetic field at which the irreversible magnetization M_{irr} vanishes, i.e., the field at which the hysteresis loop closes [21]. These data provide quantitative information on the magnetic behaviour and allow the construction of the vortex-matter $B-T$ phase diagrams shown in Figure 6e,f for the powder and core samples, respectively.

In the $B-T$ diagrams, the Meissner state is highlighted for magnetic fields below H_{C1}. On the other hand, the mixed state is established between H_{C1} and H_{C2}, where the vortices are organised into vortex-glass and vortex-liquid regimes, limited by the irreversibility line [20]. When the applied field exceeds H_{C2}, the sample transitions from the superconducting to the normal state.

It should be noted that the $H_{C2}(T)$ line shown in Figure 6e,f was estimated from the inset equation in the graph, $B_{C2} = B_{C2}(0)\left(1-\frac{T}{T_C}\right)$ [20], and is included only as a visual guide to indicate the upper boundary of the vortex-liquid regime. It should not be regarded as a direct experimental determination of H_{C2}. Here, $B_{C2} = \mu_0 H_{C2}$ [21].

A key result from the $B-T$ diagrams is the shift of the irreversibility line. For the core sample, the irreversibility line $B_{irr}(T)$ is displaced to lower temperatures and fields compared with the powder sample, as can be seen by comparing Figure 6e,f. This unfavourable shift indicates a reduction of vortex stability and a narrowing of the applicable region in the $B-T$ phase diagram. The effect is attributed to the coexistence of the 2212 phase, the presence of secondary phases and carbonate inclusions, and the resulting reduction of the effective superconducting volume and intergranular connectivity. Considering the region of applicability of the core sample is reduced, it becomes necessary to estimate the electrical transport capabilities of both the powder and core samples.

3.3.3. Critical Current Density J_C

The critical current density J_C was estimated from the $M(H)$ hysteresis loops using the Bean critical-state model. For the powder sample, the standard expression for bulk or powder samples was used [22]:

$$J_C = \frac{30\,\Delta M}{d} \tag{2}$$

where ΔM is the difference between the upper and lower branches of the hysteresis loop and d is the average grain size. For the powder sample, the average grain size was determined from the SEM micrograph shown in the inset of Figure 4a, giving $d \approx 10.5$ μm.

For the core sample, because the extracted material consists of thin flakes, the extended Bean model valid for films was applied [21]:

$$J_C(B) = \left[\frac{20\Delta M}{w\left(1-\frac{w}{3l}\right)}\right] \tag{3}$$

where w and l are the width and length of the flake, respectively. For the magnetisation measurements, a superconducting flake with $w = l =$ 4 mm was used.

Figure 6g,h show the $J_C(H)$ curves for the powder and core samples, respectively. The core sample exhibits higher J_C values than the powder sample over the entire measured temperature and field range. This enhancement is attributed to two main factors: i) the alignment of superconducting grains promoted by the thermal treatments and flat rolling improves intergranular connectivity and reduces weak-link effects. ii) the presence of secondary phases, such as Ca_2PbO_4 and carbonate-related compounds [18], can act as effective vortex-pinning centres. The combined effect of grain alignment and secondary-phase pinning leads to a significant improvement of the transport capability in the tape core.

To contextualise the performance of the fabricated tape, Table 4 compares the J_C values obtained in this work with representative J_C values previously reported for PIT-processed Bi-2223 tapes and related systems.

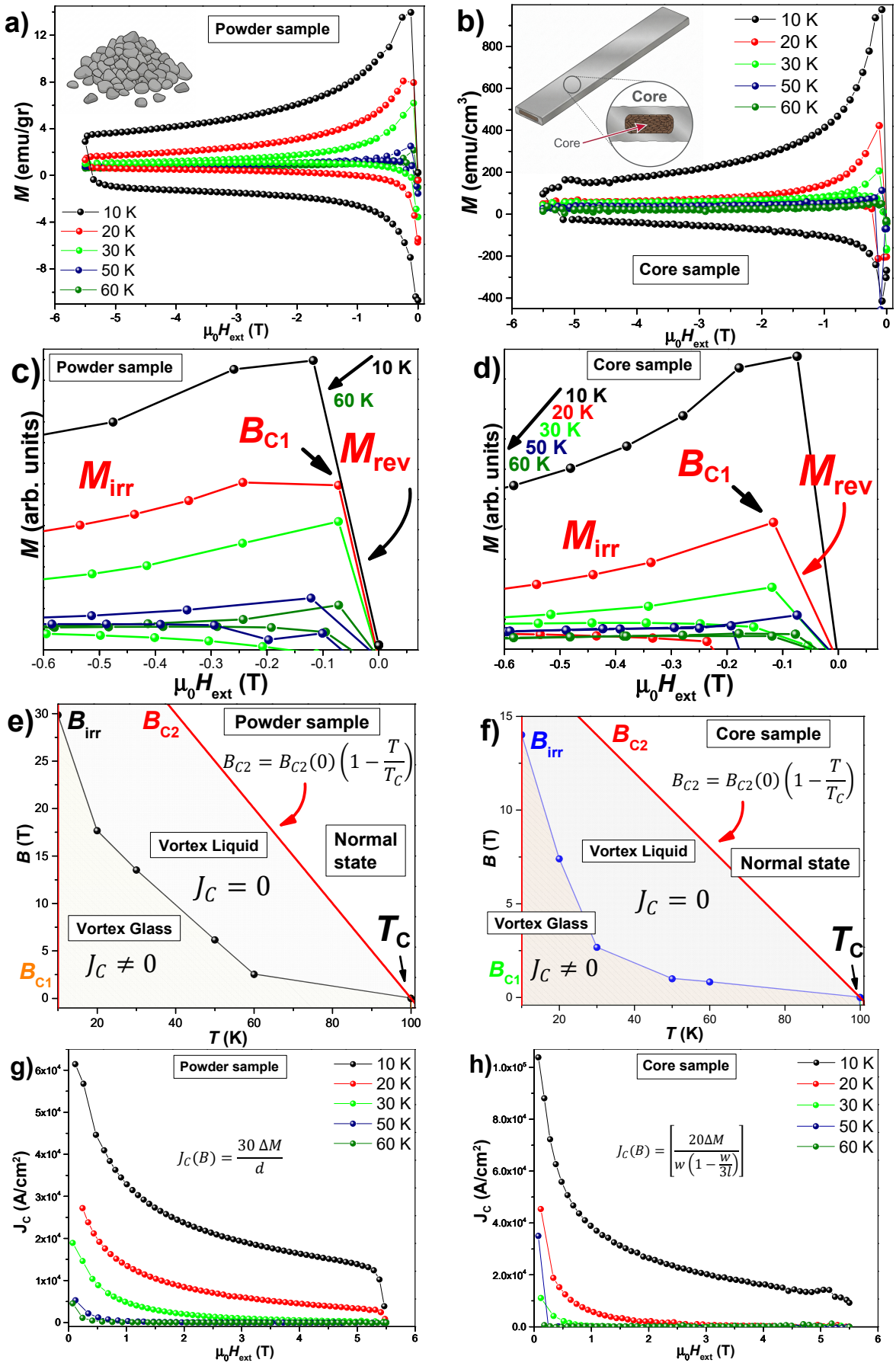


Figure 6. $M(H)$ hysteresis loops at 10–60 K for (**a**) powder and (**b**) core. (**c**) and (**d**): Low-field regions: linear reversible M_{rev} at low fields; H_{C1} is where linearity is lost and M_{irr} appears; H_{irr} is where M_{irr} vanishes. (**e**) and (**f**): $B-T$ phase diagrams for (**e**) powder and (**f**) core; the H_{C2} line (red) is a visual guide only. (**g**) and (**h**): $J_C(B)$ curves for (**g**) powder and (**h**) core, estimated from the Bean model.

Table 4. Critical current density $J_C(B,T)$ values for representative 1st-generation superconducting tapes reported in the literature.

Superconducting Phase	Experimental Details	$J_C(B,T)$ (A/cm^2)	Reference
BPSCCCO-2223	PIT method, monofilament. J_C (4.2 K, self-field)	~1.5×10^5	[5]
Bi-2223/Ag	PIT method, CCS process, monofilament. J_C (77 K, self-field)	3.05×10^4	[6]
BPSCCCO-2223	PIT method, monofilament, Pb over-doped. J_C (77 K, self-field)	2.0×10^4	[7]
Bi-2223/Ag	PIT method, experimental. J_C (77 K, self-field)	4.83×10^4	[23]
Bi-2223/Ag	PIT method, experimental. J_C (77 K, $B = 0.1$ T)	1.97×10^4	[23]
Bi-2223/Ag/Ni	PIT method, bimetallic sheath. J_C (77 K, self-field)	9.3×10^3	[24]
$(Bi_{0.8}Pb_{0.2})Sr_2Ca_2Cu_3O_{10+x}$	Solid-state reaction. PIT method. Monofilament. T_C=105 K. J_C (77 K, B =0 T)	~10^1	[25]
BiPbSrCaCuO-2223	PIT method. Multi-filamentary (61 wires). J_C (77.3 K, B =0 T)	3×10^4	[26]
BPSCCCO-2223	Solid-state reaction. PIT method. Multi-filamentary (19 wires). J_C (77 K, B =0 T)	12×10^3	[27]
BPSCCCO-2223	PIT method, monofilament. J_C (10 K, B =0.5 T)	5.5×10^4	This work
BPSCCCO-2223	PIT method, monofilament. J_C (10 K, $B = 0.07$ T)	5.3×10^5	
BPSCCCO-2223	PIT method, monofilament. J_C (10 K, B =1 T)	3.9×10^4	
BPSCCCO-2223	PIT method, monofilament. J_C (20 K, B =0.5 T)	1.2×10^4	
BPSCCCO-2223	PIT method, monofilament. J_C (20 K, B =1 T)	6.0×10^3	

3.3.4. Magnetic Relaxation

Magnetic relaxation measurements were performed to gain further insight into the vortex dynamics of the powder and core samples. While the $B-T$ phase diagrams and the $J_C(B,T)$ curves provide information on the static vortex behaviour and the transport capabilities, relaxation measurements directly probe the time-dependent motion of vortices out of their pinning positions [21,28]. This is particularly relevant in the present system because the core sample is a multiphase composite in which the 2223 and 2212 superconducting phases coexist, as confirmed by XRD and DC susceptibility. The presence of two superconducting phases with different critical temperatures and pinning forces is expected to produce a complex relaxation behaviour, which cannot be fully captured by static measurements alone.

Figure 7 shows the time-dependent decay of the normalised magnetization $M(t)/M_0$ for both samples, measured at 5 and 100 K under an applied field of 1 T. In all cases, the magnetisation decreases with time, reflecting the thermally activated motion of vortices out of their pinning centres, which dissipates the superconducting current and reduces the irreversible magnetisation.

For the powder sample (Figure 7a), the relaxation curves at 5 K and 100 K exhibit a smooth and monotonic decay. The trend of the two curves is comparable, indicating that the dominant relaxation mechanism is similar at both temperatures, just differentiate by the thermal activation of the system. The absence of any clear feature in the powder relaxation curves is consistent with the fact that the powder is essentially a single-phase 2223 material, as shown by XRD and DC susceptibility.

In contrast, the core sample (Figure 7b) exhibits a markedly different relaxation behaviour. More importantly, the curve at 5 K presents two well-defined plateaus, i.e., two regions where the magnetisation decay is temporarily slowed down. This step-like feature is a clear signature of a change in the relaxation dynamics and suggests the presence of two distinct vortex-creep regimes. The appearance of two plateaus in the core sample can be rationalised in terms of the coexistence of the 2223 and 2212 phases. Because these two phases have different critical temperatures, irreversibility lines and pinning forces, they respond differently to thermal activation.

The competition between the two phases produces a two-step relaxation process: the faster decay at short times is associated with vortices in the weaker-pinning regions, while the slower decay at longer times is associated with vortices in the stronger-pinning regions. This interpretation is consistent with the reduced T_{irr} and the shift of the irreversibility line observed for the core sample in Sections 3.3.1 and 3.3.2, and with the enhanced J_C values observed in Section 3.3.3. This provides direct evidence that the multiphase nature of the tape core not only affects the static superconducting properties but also modifies the vortex dynamics.

On the other hand, the curve at 100 K shows a rapid initial decay, attributed to the rapid rearrangement of vortices immediately after the field is applied, followed by a slower relaxation as the vortices stabilize at lower-energy positions. It is important to note that at 100 K the core sample is close to its normal state, so the vortices are not firmly pinned, unlike at 5 K. At this temperature, superconductivity is partially or completely suppressed by the external magnetic field, and the relaxation is dominated by the motion of weakly pinned vortices.

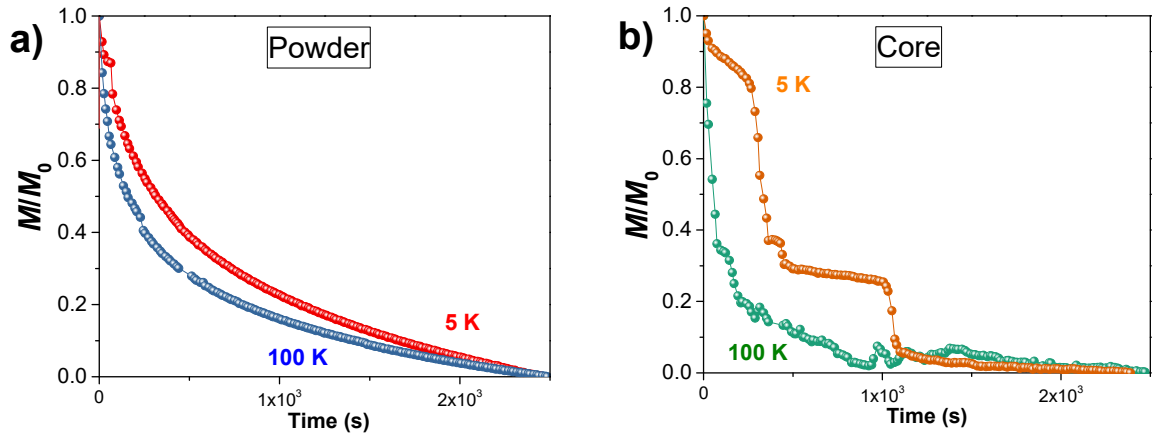


Figure 7. Magnetic relaxation curves of the powder and core samples obtained under (**a**) 5 K and (**b**) 100 K.

4. Conclusions

$Bi_{2-x}Pb_xSr_2Ca_2Cu_3O_{10+\gamma}$ superconducting tapes with coexistence of Pb-doped Bi-2223 and Bi-2212 phases were successfully fabricated by the powder-in-tube method, followed by heat treatments at 865 °C for 15 h and 810 °C for 20 h and mechanical lamination. The resulting tapes are homogeneous, with a thickness of 0.6 mm and a constant silver matrix mass, and no detectable silver diffusion into the superconducting core.

X-ray diffraction and SEM-EDS revealed that the precursor powder is mainly composed of the BPSCCO-2223 phase and a carbonate secondary phase, whereas the tape core is a multiphase composite containing the 2223 and 2212 phase, Ca_2PbO_4 and $Ca_{2.675}Cu_3Pb_{0.535}Sr_{2.675}Bi_{1.6}O_x$. The thermal and mechanical processing promoted grain growth, partial recrystallisation, flattening and alignment of the superconducting grains, together with a redistribution of secondary phases. No silver was detected in the core, confirming that the core mass can be reliably obtained by subtracting the silver matrix mass from the total tape mass.

DC susceptibility measurements showed a single superconducting transition for the powder and two transitions for the core, associated with the 2223 and 2212 phases, in agreement with the structural analysis. The irreversibility temperature T_{irr} of the core is clearly reduced with respect to the powder at both applied fields, indicating a weakening of vortex stability and a narrowing of the irreversible regime. This reduction is attributed to the coexistence of both the 2223 and 2212 phases, the presence of secondary phases and carbonate inclusions, and the resulting decrease of the effective superconducting volume and intergranular connectivity.

From the hysteresis loops, the characteristic fields H_{C1} and H_{irr} were determined, and the corresponding vortex-matter $B-T$ phase diagrams were constructed. The irreversibility line of the core is displaced to lower temperatures and fields compared with the powder, confirming the reduction of the applicable region and in agreement with T_{irr}.

The critical current density reaches values of the order of 10^5 A/cm^2 at 10 K for the tape core, which is higher than that of the powder sample over the whole measured temperature and field range. The J_C enhancement is attributed to two main factors: the alignment of superconducting grains promoted by the thermal treatments and flat rolling, which improves intergranular connectivity and reduces weak-link effects; and the presence of secondary phases, such as Ca_2PbO_4 and carbonate-related compounds, which can act as effective vortex-pinning centres.

Magnetic relaxation measurements provided further insight into the vortex dynamics. The powder sample exhibits a smooth and monotonic decay of the magnetisation, consistent with a relatively homogeneous single-phase 2223 material. In contrast, the core sample shows a complex, two-plateau decay at 5 K. This step-like feature is attributed to the competition between the coexisting 2223 and 2212 phases, which have different critical temperatures, irreversibility lines and pinning strengths. The two-plateau relaxation is therefore a fingerprint of the multiphase nature of the tape core and of its complex pinning landscape.

Author Contributions

D.A.O.T.: conceptualization, methodology, software, writing—reviewing and editing; H.E.S.C.: conceptualization, methodology, software, writing—reviewing and editing; J.G.D.: conceptualization, methodology, software, data curation, writing—original draft preparation, visualization, investigation, validation; M.J.G.: conceptualization, methodology, software, data curation, writing—original draft preparation, visualization, investigation, validation; A.G.B.D.: conceptualization, methodology, software, data curation, writing—original draft preparation, visualization, investigation, validation; J.F.S.: conceptualization, methodology, software, data curation,

writing—original draft preparation, visualization, investigation, validation; J.C.G.: conceptualization, methodology, software, data curation, writing—original draft preparation, visualization, investigation, validation; S.R.C.R.: conceptualization, methodology, software, data curation, writing—original draft preparation, visualization, investigation, validation; C.H.W.B.: conceptualization, methodology, software, writing—reviewing and editing; L.D.L.S.V.: conceptualization, methodology, software, writing—reviewing and editing. All authors have read and agreed to the published version of the manuscript.

Funding

This research was funded by the Peruvian Agency CONCYTEC-PROCIENCIA, grant number PE501097209-2025-PROCIENCIA. This work was supported by a collaboration agreement between the University of Cambridge and the National University of Barranca, contract number RG92973. DAOT acknowledges financial support for a doctoral scholarship from FAPERJ with grant No. E-26/210.742/2025 and PETROBRAS with grant No. 0050.0129649.24.9

Institutional Review Board Statement

Not applicable.

Informed Consent Statement

Not applicable.

Data Availability Statement

The datasets generated and analyzed during the current study are available from the corresponding author upon reasonable request.

Conflicts of Interest

The authors declare no conflict of interest.

Use of AI and AI-Assisted Technologies

During the preparation of this work, the authors used ChatGPT to improve the schematic representation of the step-to-step fabrication process, as noted in Figure 1. After using this tool, the authors reviewed and edited the content as needed and takes full responsibility for the content of the published article.

References

1. Bednorz, J.G.; Müller, K.A. Possible High Tc Superconductivity in the Ba−La−Cu−O System. *Z. Phys. B-Condens. Matter* **1986**, *64*, 189–193. https://doi.org/10.1007/bf01303701.
2. Maeda, H.; Tanaka, Y.; Fukutomi, M.; et al. A New High-T_C Oxide Superconductor without a Rare Earth Element. *Jpn. J. Appl. Phys.* **1988**, *27*, L209. https://doi.org/10.1143/jjap.27.l209.
3. Shimoyama, J.I.; Motoki, T. Current Status of High Temperature Superconducting Materials and Their Various Applications. *IEEJ Trans. Electr. Electron. Eng.* **2024**, *19*, 292–304. https://doi.org/10.1002/tee.23976.
4. Hayashi, K. Commercialization of Bi-2223 Superconducting Wires and Their Applications. *SEI Tech. Rev.* **2020**, *91*, 68–74.
5. Kametani, F.; Jiang, J.; Matras, M.; et al. Comparison of Growth Texture in Round Bi2212 and Flat Bi2223 Wires and Its Relation to High Critical Current Density Development. *Sci. Rep.* **2015**, *5*, 8285. https://doi.org/10.1038/srep08285.
6. Xia, S.K.; Lisboa, M.B.; Serra, E.T.; et al. Bi-2223/Ag Tapes Prepared at Temperatures above the Bi-2223 Decomposition Temperature. *Supercond. Sci. Technol.* **2001**, *14*, 103–108. https://doi.org/10.1088/0953-2048/14/2/308.
7. Pu, M.H.; Song, W.H.; Zhao, B.; et al. Enhanced Flux Pinning in (Bi, Pb)-2223/Ag Tapes by Slightly over-Doped Pb. *Supercond. Sci. Technol.* **2001**, *14*, 299–304. https://doi.org/10.1088/0953-2048/14/6/301.
8. Vadakkaathillam, G.; Sathyanarayana, A.T.; Amaladass, E.P.; et al. Evolution of Superconducting Properties of Coexistent Bi-2212 and Bi-2223 Phases in BSCCO. *Indian J. Pure Appl. Phys.* **2021**, *59*, 391–397. https://doi.org/10.56042/ijpap.v59i5.39831.
9. Ali, M.A.; Banerjee, S.S. Coexistence of Different Pinning Mechanisms in Bi-2223 Superconductor and Its Implications for Using the Material for High Current Applications. *J. Appl. Phys.* **2022**, *131*, 243901. https://doi.org/10.1063/5.0093741.
10. Mawatari, Y.; Yamasaki, H.; Kosaka, S.; et al. Critical Current Properties and Vortex-Glass-Liquid Transition in Ag-Sheathed Bi-2223 Tapes. *Cryogenics* **1995**, *35*, 161–167. https://doi.org/10.1016/0011-2275(95)93989-d.

11. Zhang, S.; Ma, X.; Shao, B.; et al. Fabrication of Multifilamentary Powder in Tube Superconducting Tapes of Bi-2223 with Sr Deficient Starting Composition. *Cryogenics* **2021**, *114*, 103245. https://doi.org/10.1016/j.cryogenics.2020.103245.
12. Wimbush, S.C.; Strickland, N.M.; Long, N.J. Low-Temperature Scaling of the Critical Current in 1 G HTS Wires. *IEEE Trans. Appl. Supercond.* **2015**, *25*, 1–5. https://doi.org/10.1109/tasc.2014.2362726.
13. Kodama, T.; Fukuda, M.; Shiraishi, K.; et al. E–J Characteristics in a Wide Range of Electric Field for a Bi-2223 Silver-Sheathed Tape Wire. *Phys. C Supercond.* **2001**, *357–360*, 582–585. https://doi.org/10.1016/s0921-4534(01)00314-8.
14. Obradors, X.; Puig, T.; Ricart, S.; et al. Progress in Superconducting $REBa_2Cu_3O_7$ (RE = Rare Earth) Coated Conductors Derived from Fluorinated Solutions. *Supercond. Sci. Technol.* **2024**, *37*, 053001. https://doi.org/10.1088/1361-6668/ad36eb.
15. Takeda, Y.; Motoki, T.; Kitaguchi, H.; et al. High I_C Superconducting Joint between Bi2223 Tapes. *Appl. Phys. Express* **2019**, *12*, 023003. https://doi.org/10.7567/1882-0786/aaf8b4.
16. Cornejo, H.S.; De Los Santos Valladares, L.; Kamboj, V.S.; et al. Texture and Terahertz Analysis of $YBa_2Cu_3O_7$ Grown onto $LaAlO_3$ by the Chemical Solution Deposition Technique. *Heat Treat. Surf. Eng.* **2022**, *3*, 1–8. https://doi.org/10.1080/25787616.2021.2022294.
17. Domínguez, A.B.; De Los Santos Valladares, L.; Cornejo, H.S.; et al. $YBa_2Cu_3O_7$ Films Grown onto $SrTiO_3$ and YSZ Substrates by Chemical Solution Deposition of Trifluoroacetates. *J. Electroceramics* **2021**, *47*, 15–22. https://doi.org/10.1007/s10832-021-00256-5.
18. Bustamante Dominguez, A.G.; Sanchez Cornejo, H.E.; González, J.C.; et al. Aging and Environmental Effects on the Superconductor $[Y_{1-x}Ca_x]SrBaCu_{2.80}(BO_3)_{0.20}O_y$ with $0.10 \leq x \leq 0.50$. *J. Supercond. Nov. Magn.* **2024**, *37*, 1903–1911. https://doi.org/10.1007/s10948-024-06745-2.
19. Cornejo, H.S.; De Los Santos Valladares, L.; Barnes, C.H.W.; et al. Texture and Magnetic Anisotropy of $YBa_2Cu_3O_7$-X Film on MgO Substrate. *J. Mater. Sci. Mater. Electron.* **2020**, *31*, 21108–21117. https://doi.org/10.1007/s10854-020-04623-w.
20. Krabbes, G.; Fuchs, G.; Canders, W.R.; et al. *High Temperature Superconductor Bulk Materials*; Wiley: Weinheim, Germany, 2006. https://doi.org/10.1002/3527608044.
21. Cornejo, H.S.; Domínguez, A.B.; Holmes, S.N.; et al. Vortex Dynamics Study on an Uniaxially Textured YBCO/MgO Superconducting Film from Magnetic Measurements. *Supercond. Sci. Technol.* **2025**, *38*, 035028. https://doi.org/10.1088/1361-6668/adb6d8.
22. Bean, C.P. Magnetization of High-Field Superconductors. *Rev. Mod. Phys.* **1964**, *36*, 31–39. https://doi.org/10.1103/revmodphys.36.31.
23. Huang, Y.B. Progress in Bi-2223 Tape Performance. *AIP Conf. Proc.* **2002**, *614*, 717–723. https://doi.org/10.1063/1.1472607.
24. Ye, C.L.; Li, M.Y.; Chen, X.P.; et al. Microstructure and Critical Current of Bimetallic Sheathed Bi-2223 Tapes. *Phys. C Supercond. Its Appl.* **2011**, *471*, 1107–1109. https://doi.org/10.1016/j.physc.2011.05.136.
25. López, M.; Mariño, A. Fabricación Y Caracterización De Cintas Superconductoras De Alta Temperatura Crítica. *MOMENTO* **2006**, 25–33.
26. Hayashi, K.; Hikata, T.; Kaneko, T.; et al. Development of Ag-Sheathed Bi-2223 Superconducting Wires and Their Applications. *IEEE Trans. Appl. Supercond.* **2001**, *11*, 3281–3284. https://doi.org/10.1109/77.919763.
27. Fischer, K.; Schubert, M.; Rodig, C.; et al. Processing, Microstructure and Critical Current Density of 2223 BPSCCO/Ag Tapes. *IEEE Trans. Appl. Supercond.* **1995**, *5*, 1259–1262. https://doi.org/10.1109/77.402790.
28. Cornejo, H.S.; Domínguez, A.B.; Holmes, S.N.; et al. Reply to Comment on '*Vortex Dynamics Study on an Uniaxially Textured YBCO/MgO Superconducting Film from Magnetic Measurements*'. *Supercond. Sci. Technol.* **2026**, *39*, 088001. https://doi.org/10.1088/1361-6668/ae97be.